Supplementary Information: Triplet and singlet state-resolved molecular dynamics in mutual neutralisation reactions of H_2^+ with H^-

Mathias Poline,[1] Arnaud Dochain,[2] Stefan Rosén,[1] MingChao Ji,[1]
Gustav Eklund,[1] Henrik Cederquist,[1] Henning Zettergren,[1]
Henning T. Schmidt,[1] Xavier Urbain,[2] and Richard D. Thomas[1,*]

[1] Department of Physics, Stockholm University, Stockholm SE-10691, Sweden.
[2] Institute of Condensed Matter and Nanosciences, Université Catholique de Louvain, Louvain-la-Neuve, B-1348, Belgium

[*]To whom correspondence should be addressed; E-mail: rdt@fysik.su.se

Supplementary Information

A brief comparison between the two experimental facilities and their operation is discussed. In order to evaluate the data, appropriate methods must be used to determine the momentum vectors and energies of the products, and Monte Carlo simulations of the particles trajectories must be implemented. The reaction can in principle lead to both two- and three-body products, and these are treated independently to determine the product branching fractions. The theoretical treatment is presented in detail, as are the methods used to determine the emission spectra, together with the collision energy dependent cross-sections and rate coefficients.

Supplementary Note 1: Materials and Methods

Supplementary Note 1.1: Merged beams

The current best method for determining the products distribution in an MN reaction is the three-dimensional imaging technique. The kinetic energy released in the reaction results in a recoil of the particles relative to their centre of mass, which can then be directly measured in the lab frame. For an MN event taking place at a distance L from a detector, with ions moving at speed v, the centre-of-mass kinetic energy of a product with mass m is given by:

$$E = \frac{v^2}{2L^2} m |\vec{r}^{\,2}|, \tag{1}$$

where $\vec{r} = (\Delta x, \Delta y, v\Delta t)$ is position of the particle relative to centre-of-mass passing the detector plane. Coincidence measurements allow us to determine the number of products, and the sum of each product's energy yields the final kinetic energy released in the reaction E_{K_f}.

To achieve this, merged ion-beams setups have been proven to be the most effective tool.

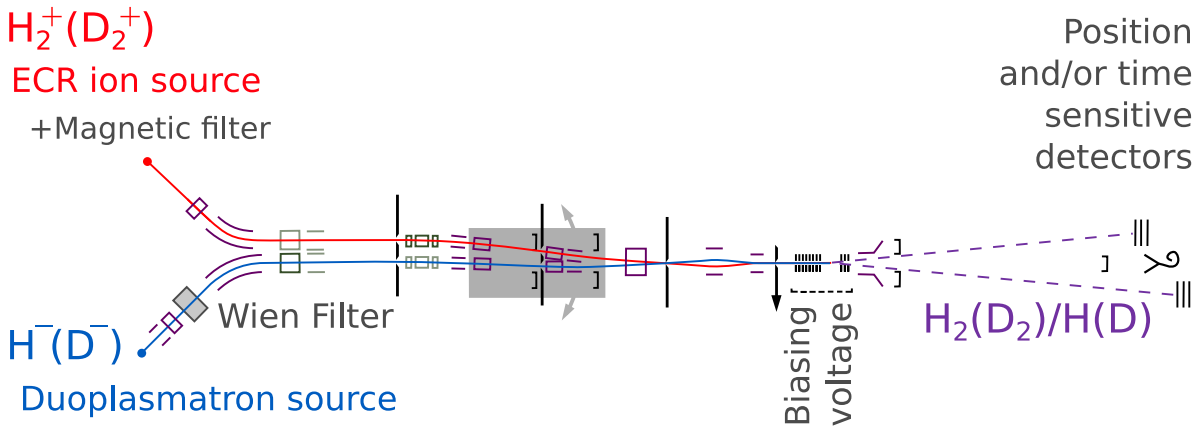

Supplementary Figure 1: Schematic of the UCLouvain experimental apparatus. Anion and cation beams are shaped using 1 mm apertures. The detection system consists of two triple-stack MCPs backed by a resistive anode and a channel electron multiplier for the three-body coincidences.

They ensure well-characterised reactants and control over the collision energy while they take advantage of the high particle speed for efficient detection of the products. There are currently two such experimental apparatus in the world: the UCLouvain single-pass merged beam apparatus (*1*) as shown in Supplementary Fig. 1, and the double electrostatic ion-beam storage ring, DESIREE, in Stockholm (*2, 3*) in Supplementary Fig. 2.

The main difference between them resides in their different capabilities to store the ions prior to their interactions. The two setups come with their own different advantages and disadvantages: The single-pass method allows exquisite control over the alignment and collision energy, thereby offering a high resolution, $\Delta E_K/E_K \simeq 1\%$ (*4*). However, since the ions are not stored, their electronic and rovibrational energy distribution remains close to those in the ion source. This makes the interpretation of the data challenging due to overlapping distributions in the kinetic energy release spectra. The cryogenic storage ring technique such as the one used in DESIREE, is therefore generally more suitable for the study of MN involving molecular ions,

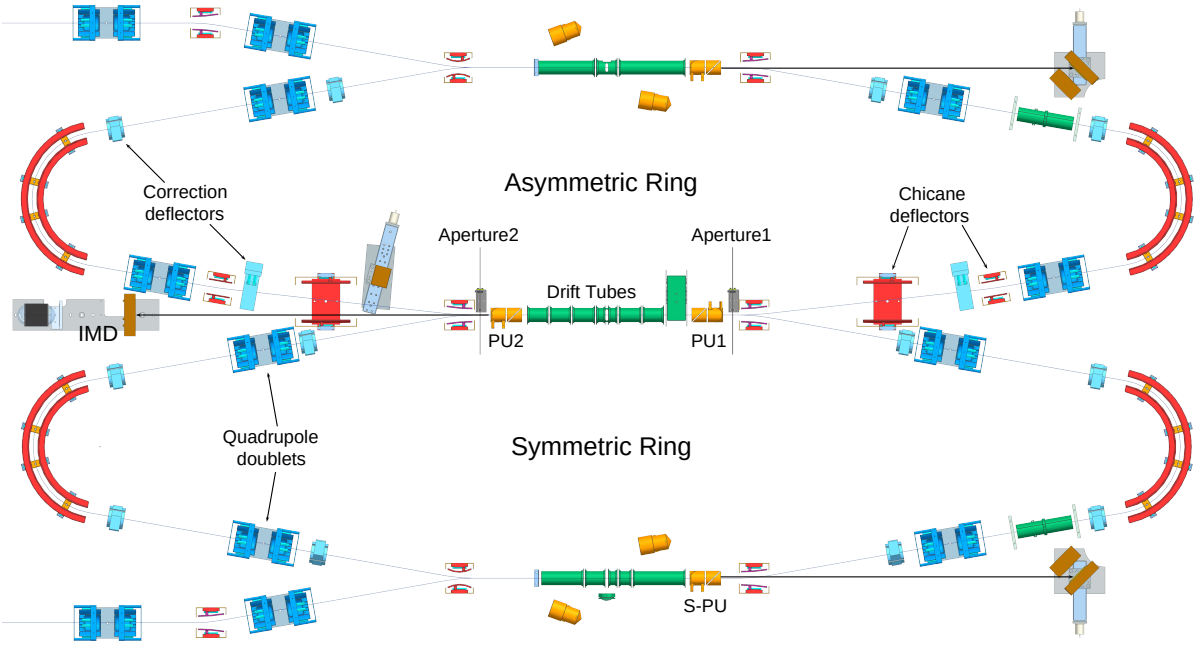

Supplementary Figure 2: Schematic of the experimental setup at DESIREE. The two oppositely charged ion beams are injected and stored in their respective rings by the use of quadrupoles and deflectors. Between the two pick-up (PU) electrodes, they are merged together and interact freely. The neutrals formed in the MN reactions continue straight to the imaging detector (IMD).

since the ions can cool down radiatively to the cold environment, preparing a much narrower initial quantum state distribution, ideally a single quantum state, see e.g. (*5*). For D_2^+, this is not the case as there is no intrinsic dipole moment and so the ions remain rovibrationally hot, even in a cryogenic environment, and the single-pass method is preferable (here D_2 was chosen rather than H_2 to maximise detection efficiency). In contrast, HD^+ quickly cools into its vibrational ground-state in about 50 ms, though the radiative lifetimes of the J=1-7 rotational levels in this state are longer; ≈140 s to ≈0.3 s, respectively (*6*). The two different experimental apparatus were therefore used to study the two reactions of interest, namely the MN of hot D_2^+ or cold HD^+ with D^-.

For each injection in the single-pass measurements or during each orbit in the storage ring measurements, the ions are merged, overlapped, and passed co-linearly through a common interaction region before being de-merged. In the single-pass apparatus (*4*), this region is defined by a set of plates with a centre hole and a 6 mm spacing, individually biased, whilst in the storage ring (*7*) this is a set of seven drift tubes. The ion beam energies are chosen such that the relative collision energy between the two beams is high, i.e., > 20 eV whilst the collision cell/drift tubes are at ground potential, i.e., unbiased. Applying a bias voltage to the cell or drift tubes accelerates and decelerates the anions and cations, respectively, such that their relative velocity decreases significantly, and collision energies of $E_{coll} < 100$ meV are achieved. Neutralised particles formed in this biased drift region are not deflected, and travel in straight trajectories to the time-and-position sensitive neutral particle detector(s). Neutralised particles formed in any unbiased part of the interaction region have significantly larger arrival time difference distributions, and can be filtered out.

In the single-pass apparatus (Supplementary Fig. 1), coincident two-particle events are de-

tected by two separate detectors, each consisting of a triple-stack of microchannel plates (MCPs) and a resistive anode, which can register both the position and time-of-arrival. For the purpose of this experiment, and to measure dissociative MN reactions, an additional channel electron multiplier (CEM) was placed in-between the two MCP-based detectors to allow coincident detection of these events. However, the CEM can only register the particle's time-of-arrival, and the position is deduced from analysing the centre-of-mass of the two other products. As a result, the energy resolution of the fully dissociative channel is significantly reduced compared to the non-dissociative channels as can be seen by comparing Figures 1c and 1f in the main text.

In DESIREE (Supplementary Fig. 2), a single, triple-stack-MCP-phosphor-screen based detector is used, from which the light from the phosphor is coupled out of the vacuum and recorded by a pixel-sensitive camera (TPX3CAM, see e.g., (*7–10*)). The camera can effectively register any number of events, as long as separate pixels are triggered. As such, the resolution is instead limited by the length of the interaction region required to gather sufficient statistics, which can be expressed as a range of possible distances, $L = 1.78 \pm 0.12$ m, between low-energy MN-events and the detector. This gives a similar resolution as for the single-pass three particle data, i.e., $\Delta E_K/E_K \simeq 3\%$

Supplementary Note 2.0: Data evaluation

In order to evaluate the data, appropriate methods must be used to determine the momentum vectors and energies of the products, and Monte Carlo simulations of the particles trajectories must be implemented. The reaction results in both two- and three-body products, and these are treated independently. We restrict here the analysis to the $HD^+ + D^-$ system. In principle, the same procedures are applied to the $D_2^+ + D^-$, with some variations given the difference between the two systems.

Supplementary Note 2.1: Three-body and intermediate capture-state analysis

In the fully dissociative process for cold HD^+ ions, only one channel is energetically allowed, namely:

$$\mathrm{HD}^+(^2\Sigma) \quad + \quad \mathrm{D}^-(^1\mathrm{S}) \qquad \rightarrow \qquad \mathrm{H}(^2\mathrm{S}) \quad + \quad \mathrm{D}(^2\mathrm{S}) \quad + \quad \mathrm{D}(^2\mathrm{S}) \quad + \quad \Delta E, \quad (2)$$

where $E_{K_f} = \Delta E = 10$ eV provided that no energy is dissipated from the system before the final state, with three H-atoms in their ground state, is reached. Here, given the products have different masses, the particles must first be identified in order to determine their kinetic energy. This is achieved by evaluating the centre-of-mass for all permutations of the three-particle products. The identity of the products is then assigned by selecting the permutation which lies closest to the centre-of-mass of the two beams. This allows to deduce an actual experimental value for the total kinetic energy release, E_{K_f}, of the three products. The obtained distribution for all three-body events is indicated by the black filled circles, plotted with statistical uncertainties, in Supplementary Fig. 3a. Analysis of the spectra clearly indicates that the observed distribution does not match the expected energy of 10 eV for reaction channel 2, but rather peaks at an energy of ~ 4 eV. To elucidate this, we also evaluated the break-up dynamics using the standard mass-weighted Dalitz coordinates, according to:

$$\eta_1 = \frac{1}{3}\sqrt{\frac{M}{m_H}}\left(\epsilon_{D_1} - \epsilon_{D_2}\right) \quad (3)$$

$$\eta_2 = \frac{1}{3}\left(\left(1 + \frac{m_H}{m_D}\right)\epsilon_H - \epsilon_{D_1} - \epsilon_{D_2}\right) \quad (4)$$

where ϵ_H is the fraction of energy taken by the hydrogen atom, and $\epsilon_{D_1}/\epsilon_{D_2}$ the fraction taken by the two deuterium atoms. This allows to confine all possible configurations of energies within

a triangle, with the allowed configurations restricted within a circle due to momentum conservation. The result is shown in Supplementary Fig. 3b.

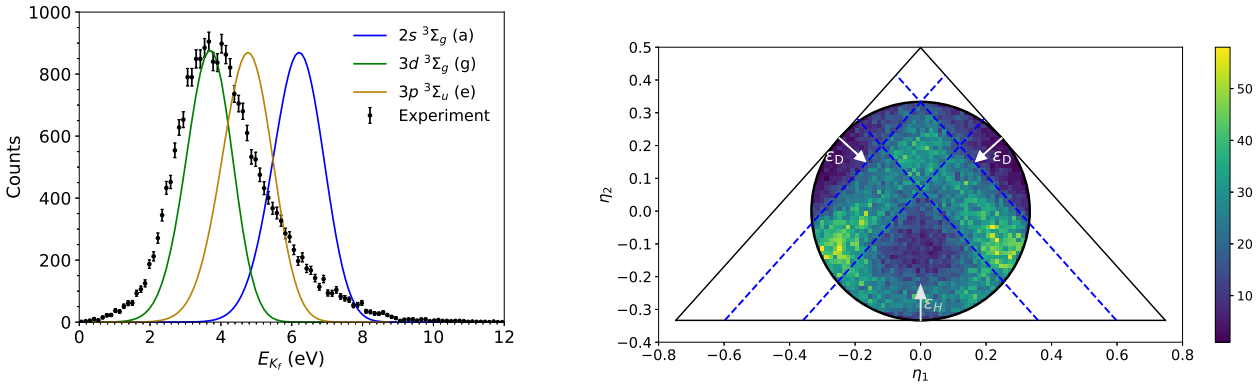

(a) (b)

Supplementary Figure 3: Three-particle data for the $HD^+ + D^- \rightarrow HD^* \rightarrow H + D + D$ reaction. (a) Kinetic energy release, E_{K_f} distribution. The experimental data, black filled circles, are plotted with statistical uncertainties. Simulated distributions for a few selected intermediate electronically excited HD^* capture states which couple to the same final dissociative state are shown as coloured lines. (b) A Dalitz plot showing the kinetic energy received by the three fragments, with the energy fraction of each product shown by the white arrows while the blue lines highlight the relevant features.

The axis of the energy fraction ϵ of each particle is depicted by the arrows, and the plot is symmetric due to the D atoms having the same mass. The Dalitz plot reveals most events are concentrated to two broad strips (highlighted by the blue lines), parallel to the triangle's sides. Such features indicate the D atoms only receive a restricted fraction of the available kinetic energy, which is consistent with a two-step process in which the most loosely bound electron in D^- is first transferred to form excited HD which breaks up later. here, the timescale for this fragmentation is long compared to the collision time but short compared to the flight time to the detector. This can be described in the following way:

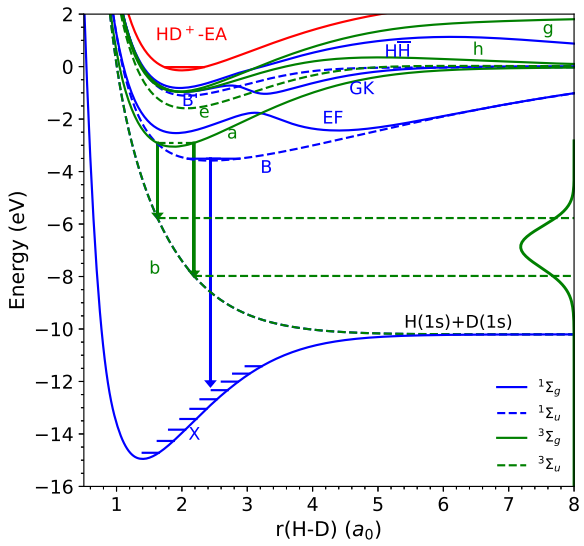

Supplementary Figure 4: Potential energy curves for the $HD^+(^2\Sigma_g^+)$ ionic ground-state, and several selected states of HD with $^1\Sigma_{g/u}$ and $^3\Sigma_{g/u}$ symmetry. The HD^+ potential has been shifted by the electron affinity of H such that the energy differences correspond to the kinetic energy released in the mutual neutralisation reaction.

$$HD^+(^2\Sigma) + D^-(^1S) \rightarrow HD^*(^3\Lambda) + D(^2S) + E_{K_i} \rightarrow H(^2S) + D(^2S) + D(^2S) + E_{K_f}, \quad (5)$$

where E_{K_i} is the intermediate kinetic energy release due to the first step (electron transfer). In HD (and H_2), only the triplet states can couple to the dissociative potential. This can either occur directly, via couplings between HD^* and H+D potential energy curves (predissociation) or radiatively, as the excited HD^* (or H_2^*) states decay down to the dissociative state. Here, the results reveal that only the latter takes place: the E_{K_f} distributions namely present no clear features at 10 eV, and the observed distribution is instead consistent with an energy loss via photo emission.

The observed broad energy distribution can be understood from the available potential energy curves of H_2, as depicted in Supplementary Fig. 4 for the Σ-states. Here, we take the

decay from the a $^3\Sigma_g$ state as an example, where the green vertical arrows indicate emitted photons. The photon energy varies depending on where the wavepacket describing motion on the a $^3\Sigma_g$ potential is when the decay occurs. This is directly related to the Franck Condon overlap between the a $^3\Sigma_g^+$ state and the final dissociative b $^3\Sigma_u$ state. As such, the photon energy distribution is a projection of the vibrational wave function onto the dissociative b $^3\Sigma_u$ potential. The kinetic energy released for three products is then the total energy available (10 eV) minus the photon energy, which itself then also becomes a broad energy distribution. These distributions can be simulated by computing the vibrational wavefunctions of relevance. For a few selected states, these data are plotted in Supplementary Fig. 3a.

While the distribution is consistent with reaction proceeding by capture into the $3d\ ^3\Sigma_g$ state (see Supplementary Fig. 3a), contributions from other electronic states cannot be ruled out. However, making an appropriate fit is difficult due to the overlapping distributions. Furthermore, production of vibrationally excited HD in the electron-transfer step of the reaction can not be ruled out, which requires that more complicated distributions must also be included in the fitting procedures.

Given the observed sequential MN-reaction process, the free-rotor model may be applied (*10,11*), which implies the intermediate state survives for a time period exceeding one rotational period. Thereby, the neutralised anion no longer participates in the reaction after the initial electron-transfer step, i.e. no further energy is then exchanged between D and HD*. The fraction of the available energy taken by the neutralised anion is therefore determined by the kinetic energy, E_{K_i}, released as the intermediate state is formed. Here, and from conservation of energy and momentum, this is determined by the kinetic energy of the neutralised anion:

$$E_{K_i} = \frac{m_{HD} + m_D}{m_{HD}} E_{D_{\text{anion}}} \tag{6}$$

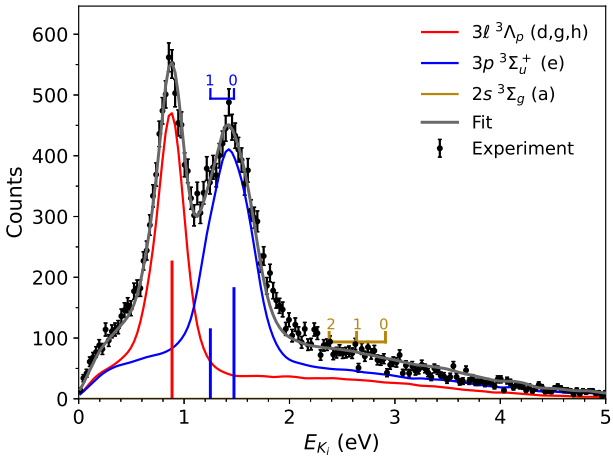

Supplementary Figure 5: Intermediate kinetic energy release distribution, E_{K_i}, for the $HD^+ + D^- \rightarrow HD^* + D \rightarrow H + D + D$ reaction

This result is exact provided that the neutralised atomic anion can be correctly identified among the three atoms. The main task is therefore to identify the neutralised D^- product from the two D products. To achieve this, we select the D atom with the lowest kinetic energy. This selection is motivated by the fact that the H+D products receive an additional kinetic energy as the HD molecule decays to the dissociative state. As such, the D atom from the H+D products most often receive more energy. This then allows to determine the intermediate kinetic-energy release spectrum, E_{K_i}, associated with the first step in eq. 5, and this data is plotted in Supplementary Fig. 5.

Since this selection is not perfect, a background is associated with the distribution. While two peaks can be observed, there is an associated tail to lower and higher energies due to misidentification of the D atom. Another cause of misidentification comes from the spread in the centre-of-mass distribution of the events, which results in the particles sometimes being assigned the wrong mass. This can be observed in the Dalitz plot shown in Supplementary Fig.

3b, where an additional faint band is observed for the H atom.

In order to reproduce these data in our simulation, these two effects must be taken into account. First, we apply the free-rotor model in order to generate events which describes the reaction taking place correctly. The momentum vectors in such a model are given by:

$$\begin{aligned} \bar{p}_{D1} &= (-p, 0) \\ \bar{p}_{D2} &= \left(\frac{m_{\mathrm{H}}}{m_{\mathrm{HD}}} p + \Delta p \cos\theta, \Delta p \sin\theta \right) \\ \bar{p}_{H} &= \left(\frac{m_{\mathrm{D}}}{m_{\mathrm{HD}}} p - \Delta p \cos\theta, -\Delta p \sin\theta \right) \end{aligned} \quad , \tag{7}$$

where

$$\begin{aligned} p &= \sqrt{\frac{2 m_{\mathrm{HD}} m_{\mathrm{D}}}{m_{\mathrm{HD}} + m_{\mathrm{D}}} E_{K_i}} \\ \Delta p &= \sqrt{\frac{2 m_{\mathrm{H}} m_{\mathrm{D}}}{m_{\mathrm{H}} + m_{\mathrm{D}}} \Delta E} \end{aligned} . \tag{8}$$

Here, θ is the angle between the HD-dissociation axis and the recoil momentum vector from the electron transfer step of the reaction and ΔE is the difference in energy between the intermediate molecular state and the dissociation limit, minus the photon energy. This is done for the three classes of states which are separated well enough in energy, i.e the $^3\Sigma_u$ (e) state, the 3ℓ $^3\Sigma_g^+$ (g,h), and the $2s$ $^3\Sigma_g$ (a) state. The effect of mass-misidentification is taken into account by including a spread in the centre-of-mass in the simulations, and then applying the same procedure as done experimentally to identify the masses. The resulting simulated distributions are shown in Supplementary Fig. 5 as coloured lines, with the grey line indicating the fit to the experimental data. Analysis indicates that the simulations describe rather well the experimental data.

In the simulations we have included all vibronic states that are predicted by our calculations to be populated by more than 1%. The vertical bars indicate the populations for these states.

From these, we see that the $3p\ ^3\Sigma_u$ (e) state and the $3\ell\ ^3\Lambda_p$ (d,g,h) states contribute to the observed spectra, while the 2s $^3\Sigma_g$ (a) state does not. Instead, the features at energies above 2-3 eV are found to be due to misidentification of the products. The distribution arising from particle misidentification is simulated independently, then subtracted from this spectrum to obtain the E_{K_i} spectrum shown in the main text. The data from the experimental observations, and the fits from the simulations, for capture into the intermediate states in HD, and their proposed fluorescence down to the fully dissociative final state, are collected in Supplementary Table 1.

Supplementary Table 1: Branching from the fit of simulated distributions shown in Supplementary Fig. 5 to the intermediate capture states in HD, and their proposed fluorescence, before dissociating. Only vibronic states with theoretical populations of $> 1\%$ are shown, remaining states are clustered as "Others".

Intermediate HD capture state	E_{K_i} (eV)	Branching Theory	Branching Experiment	Fluorescence scheme
$2s\ ^3\Sigma_g^+$ (a, $v=2$)	3.0	3.2	<1	a → b
$3p\ ^3\Sigma_u^+$ (e, $v=0$)	1.47	35.4	34.9 ± 1.7	e → a → b
$3p\ ^3\Sigma_u^+$ (e, $v=1$)	1.25	8.3	21.9 ± 1.1	e → a → b
$3s\ ^3\Sigma_g^+$ (h, $v=0$)	0.86	11.1		h → b
$3p\ ^3\Pi_u$ (d, $v=0$)	0.85	17.0 } 46.5	} 43.3 ± 3.1	d → a → b
$3d\ ^3\Sigma_g^+$ (g, $v=0$)	0.81	18.4		g → b
Others	-	6.8	-	

Supplementary Note 2.2: Two-body analysis

In a non-dissociative process, both products receive a fixed amount of kinetic energy, and simulation of the momenta vectors is straightforward (see, e.g. (*10, 12*)). The final kinetic energy release is calculated using equation 1 for the coincidence two-particle events. The resultant experimental E_{K_f} spectrum for the MN of HD^+ with H^- is shown in Supplementary Fig. 6. Here, a different distribution related to background contributions in observed: as the MCP detection efficiency is not 100%, three-body events in which one particle is not detected, but which still

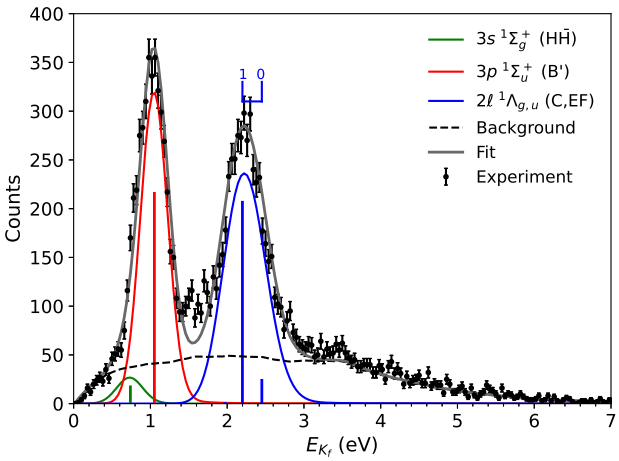

Supplementary Figure 6: Kinetic energy release distributions, E_{K_f}, for the non-dissociative product coincidence data. The experimental data are indicated by the filled black circles. The thin grey dashed line plots the contributions from three-body data where one neutral product is randomly removed, and the solid red and blue lines plot the remaining two-body coincidence data.

satisfies centre-of-mass filtering, contribute to the two-body E_{K_f} data. This contribution can be evaluated by randomly selecting two products out of the three from the three-body data presented earlier, and these data are indicated by the dashed grey line plotted in Supplementary Fig. 6.

Here, and similarly as was done for the fully dissociative reaction, only vibronic states with a predicted population of $>1\%$ were included. The fit reveals the reaction predominantly forms HD in the $3p\ ^1\Sigma_u$ (B′) and $2\ell\ ^1\Lambda_p$ (C, EF) states. Additionally, we find that the latter mainly is populated in the $v = 1$ state, as mentioned in the main text. Supplementary Table 2 collects the experimental and simulated data together with the expected fluorescence.

Supplementary Table 2: Branching from the fit of simulated distributions shown in Supplementary Fig. 6 for non-dissociative MN reactions, as well as their proposed fluorescence. Only vibronic states with theoretical populations of $> 1\%$ are shown, with remaining states gathered together as "Others".

		Branching		
Stable HD capture state	E_{K_f} (eV)	Theory	Experiment	Fluorescence scheme
$2p\ ^1\Pi_u$ (C, $v = 0$)	2.41	3.6	5.2 ± 1.6	C $\rightarrow$ X
$2s\ ^1\Sigma_g^+$ (EF, $v = 0$)	2.40	12.3		EF $\rightarrow$ B $\rightarrow$ X
$2p\ ^1\Pi_u$ (C, v =1)	2.16	11.5	44.6 ± 1.9	C $\rightarrow$ X
$2s\ ^1\Sigma_g^+$ (EF, $v = 3$)[1]	2.15	28.1		EF $\rightarrow$ B $\rightarrow$ X
$3p\ ^1\Sigma_u^+$ (B′, $v = 0$)	1.00	21.5	46.5 ± 1.3	B′ $\rightarrow$ X,EF $\rightarrow$ X
$3s\ ^1\Sigma_g^+$ (H$\overline{\text{H}}$, $v = 0$)	0.79	3.6	3.7 ± 1.9	H$\overline{\text{H}}$ $\rightarrow$ B,C $\rightarrow$ X
Others	-	7.8	-	

[1] $(EF, v = 3)$ corresponds to v = 1 of the inner potential well.

Supplementary Note 2.3: Extracting total branching ratios

The partial branching ratios from the two experimental distributions are retrieved by peak-fitting Monte Carlo simulations of the kinetic energy release to the experimental data, as described previously. Here, given the observation of both two-particle and three-particle events, the MCP detection efficiency ϵ must be evaluated in order to obtain the total branching ratios. The contribution from the three-particle data to the two-particle data is used to infer this: the probability to detect two products in a three-particle event is given by $3\epsilon^2$(1-ϵ), compared with ϵ^2 for a two-particle event and ϵ^3 for a three-particle event. This results in a background in the two-particle data. By fitting this background, one obtains the number of two-particle events, N_{23}, arising from the three-particle data, N_{33} as:

$$\frac{N_{33}}{N_{23}} = \frac{\epsilon^3}{3\epsilon^2(1-\epsilon)} \Rightarrow \epsilon = \frac{3\frac{N_{33}}{N_{23}}}{\frac{N_{33}}{N_{23}} + 1} = 0.41 \pm 0.03 \tag{9}$$

This then allows to calculate the branching ratio between the two outcomes, which are shown in Table 1 in the main text. Here, given that the fit is highly sensitive to the exact energies of

each vibronic state, we only report the total branching ratio for each class of electronic states.

Supplementary Note 2.4: Photon emission spectrum

Given the relatively good agreement between experiment and theory, the branching ratios from the theoretical calculations may be used to produce a predictive emission spectrum of the H_2^+ + H^- reaction. These calculations yield the populations of each vibronic state, for which the expected photon wavelengths can be calculated. Here we use the compilation of calculations by U. Fantz and D. Wünderlich (*13*) to determine the resulting cascade of the optically allowed transitions. Note that some transitions are not shown here: The E→B transitions which are in the microwave region, and the vibronic states with population less than 1% are neglected. The distributions were convoluted with an arbitrary width of 5 nm.

Supplementary Note 3.0: Theoretical framework

The full quantum approach is time consuming and computationally intensive, especially if a molecule is involved, as it requires evaluating every possible potential energy surface along the different reaction coordinates, i.e, the angle and separation between the H_2 molecule and the hydrogen atom need to be considered in the present case. The asymptotic model is more straightforward to extend to MN involving diatomic molecular cations, and Supplementary Fig. 7 illustrates how this is implemented in the present study. The reaction dynamics described here remains similar to the asymptotic atom-atom picture – with modifications listed below – where the electrons from the outermost orbitals in the electronic configuration of the two collision partners are used to determine the wavefunctions involved in the electron transfer process between the atomic anion and the molecular hydrogen cation. Therefore, the diatomic potentials are used only to determine the vibrational level energies and the associated Frank-Condon

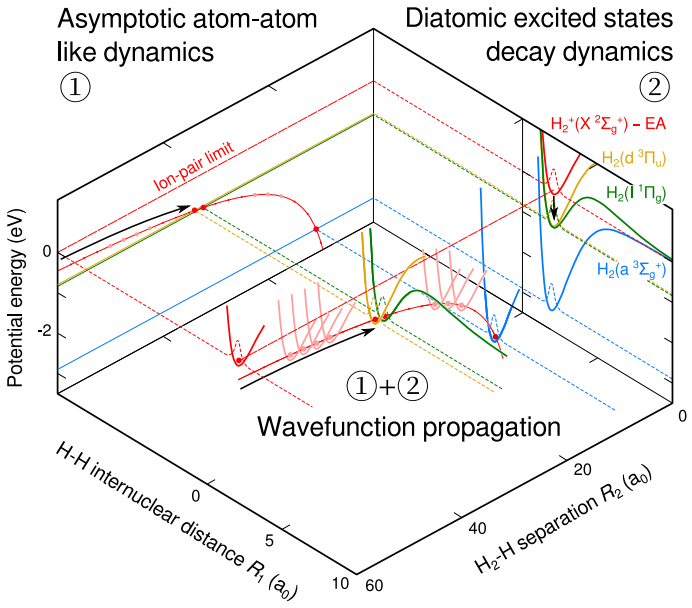

Supplementary Figure 7: Schematic of the theoretical model for an MN reaction involving a molecular cation. To the right: A subset of potential energy curves of H_2 and H_2^+ – shifted by the electron affinity EA of H^- – (plain curves) combined with their first vibrational wavefunction – shifted by the energy of the vibrational level (dashed lines). The latter are reported to the left panel which defines the H_2-H covalent energy levels and the ion-pair limit where the H_2^+-H^- distance is infinite (long dash), the $1/R_2$ separation dependency of this ionic potential is indicated by the plain red curve. The red dots indicate the crossing between the ionic and covalent curves. The central panel combines the two approaches at the same time: it shows the H_2^+-H^- potential energy surface and the associated vibrational energy at various R_2 distances, meaning that the surface is slightly below the ionic curve at all distances. At the crossings, the H_2-H potential energy surface and the first vibrational wavefunction are displayed; they are considered independent of R_2.

factors between the cation and the neutral state. Also, in later steps, they are used to describe the final states decay dynamics.

The first hypothesis of the asymptotic atom-molecule model is the sequential character of the process, i.e., electron transfer first, emission and/or dissociation second and/or third. It allows to split the calculation into two parts (Supplementary Fig. 7), each of which is treated separately:

1. The outermost electron in H^-/D^- is transferred to the molecular cation and forms a neutral molecule in a Rydberg state. This is a vertical capture process, i.e., it is faster than a single vibration of the molecule, which typically lasts several femtoseconds.

2. The excited H_2 neutral molecule either radiatively decays to either a dissociative or (meta)stable state. These processes, as described in the previous section, are slower and typically occur on the nanosecond timescale.

The natural description of the system is given using Jacobi coordinates, where R_1 is the internuclear distance between the two atoms of the parent cation, and R_2 is the distance between the centre-of-mass of the molecular cation and the anion. This description decouples the problem into two parts for trajectories where $R_1 << R_2$ where R_1 is about one Bohr radius, and R_2 typically is greater than ten Bohr radii for the MN-reactions considered here. Therefore, during the first, electron-transfer part of the collision, the diatomic molecule is considered as a compact object i.e., nearly an atom whose energy levels are the vibronic levels. As a consequence, only few small modifications are required to extend the semi-classical treatment of charge transfer in atom-atom collision (*14, 15*) to systems where diatomic molecules interact with atoms.

The atom-atom scheme used as a starting point (*1*) describes the neutralising collision using a multi-channel Landau-Zener model (*14–16*), where the probability of a transition between the diabatic ionic potential energy curve and a covalent potential energy curve is given by the following expression:

$$p_{\mathrm{atom}} = 1 - \exp\left(\frac{-2\pi E_{ic}^2}{v_{R_2}|d(V_{\mathrm{i}} - V_{\mathrm{c}})/dR_2|_{R_2=R_x}}\right) \tag{10}$$

where v_R is the relative radial velocity of the two reactants, and E_{ic} is the electronic coupling matrix element. The ionic potential is approximately described by

$$V_{\mathrm{i}} = V_{\mathrm{as}} - \frac{1}{R_2} - \frac{\alpha}{2R_2^4} \tag{11}$$

where $V_{\rm as}$ is the asymptotic energy of the ion-pair state, and α is the polarisability of the system. The covalent pair potential is assumed to be flat in the region of the crossings.

The total transition probability, P_n, to reach a given final state n combines all the paths through the various crossings that couple to that state. To keep the model simple, interferences between all those paths are neglected. Under this assumption, the collision is described using an impact parameter, b, where the partial cross section for populating the final channel n is obtained by integrating over all the trajectories (*17*):

$$\sigma_n = 2\pi \int P_n(b)\ b\ db \tag{12}$$

The main challenge in the evaluation of this model arises from calculating the interaction term E_{ic}, in equation (10). To achieve this, a newly developed anion-centred asymptotic model (ACAM) is used (*1*). This model employs a linear-combination-of-atomic-orbitals (LCAO) type approach, in which only one active electron shell for the neutralized atom and one active shell for the anion is considered. In addition, only the asymptotic exponential part of the radial wavefunction is used. Using the Landau-Herring (*18*)/Firsov integral (*19*) method, the interaction between the ionic and covalent wavefunctions is given by

$$E_{ic,ACAM} = \langle \psi_i | H | \psi_c \rangle = \oint_S \mathscr{W}(\psi_i, \psi_c)\ d\vec{S}, \tag{13}$$

where the integration is performed on a spherical surface S centred around the anion core, where $\mathscr{W}$ is the Wronskian (*20*), whose result does not depend on the size of the sphere as long as it satisfies the asymptotic condition. This method works as long as the distance between the the two reactants is larger than the non exponential component of the neutralized cation wavefunction. The validity of this approximation was previously discussed in (*12*).

A modification of this asymptotic model, suggested by Liu *et al.* (*21*), is used also here but in a slightly different way. As the transition between the ionic and the covalent state is rapid, the transition probability is governed by the overlap between the ionic and the neutral vibrational wavefunctions whose quantum numbers are v_+ and v_0, respectively, embodied in the Frank-Condon factor $FCF(v_+, v_0)$. Then equation 10 is replaced by:

$$p = p_{\text{atom}} FCF(v_+, v_0) \tag{14}$$

A second modification, which we introduce, concerns the effect of the relative orientation of the diatomic molecule. Its Rydberg states are described as $n\ell\lambda\ ^{2S+1}\Lambda_{g,u}$ configurations, where $\Lambda = \|\tilde{\Lambda}\|$ is the projection of the orbital angular momentum L along $\vec{R}_1$, and $\lambda = \|\tilde{\lambda}\|$ is the projection of ℓ along the same axis. For $H_2(1sn\ell)$ Rydberg states, $\tilde{\Lambda} = \tilde{\lambda}$ and $L = \ell$. This projection axis differs from the one used in the atom-atom collision, where the m_ℓ projection of ℓ along $\vec{R}_2$ is preserved by the charge exchange i.e., interaction terms between ionic and covalent states are non-zero only in those cases. Therefore, one needs to project $\tilde{\lambda}$ on $\vec{R}_2$ using the Wigner small-d matrix, $d^l_{\tilde{\lambda},m_l}(\theta)$ where θ is the angle between $\vec{R}_1$ and $\vec{R}_2$. As a result, the interaction terms become:

$$E_{ic} = d^l_{\tilde{\lambda},m_l}(\theta) E_{ic,\text{ACAM}} \tag{15}$$

The angle θ is evaluated using the impact parameter approach, i.e., at the beginning of the collision the molecule is randomly oriented (fixed for all impact parameters) then the deflection is evaluated for each R_2 by integrating the trajectory. Once all the interaction terms are calculated, the transition probabilities are obtained using the multi-channel Landau-Zener model (integrated over all impact parameters) and averaged for several molecular orientations (Monte-Carlo method). Therefore, even if H^- transfers a $1s(m_\ell = 0)$ electron, in addition to the expected H_2 Σ Rydberg states, H_2 Π and Δ Rydberg states can also be formed. Furthermore, this method allows transitions to either gerade or ungerade states: such transitions are not in-

cluded in the approach considered by Liu *et al* (*21*). This idea was initially proposed by Larson and co-workers (*22*) who noted that the H_2^+ + H^- collisions are not well described if $\theta = 0$ and $\pi/2$ are the only angles considered.

The modification considered here is based on the fact that the diabatic $1s\sigma n\ell\lambda\ ^1\Sigma_g^+$ states are mixed with the $2p^2\ ^1\Sigma_g^+$ state, leading to double-well PESs, such as the EF and $H\overline{H}$ adiabatic states shown in Fig. 1 in the main text. The electronic configuration differs in each well, and the vibrational wavefunction determines the configuration mixing for each vibrational level. In the current model, only the configuration with the highest interaction term is kept: this approximation is valid as the interaction term associated with the $2p^2$ configuration is null and the $1s\sigma nd\sigma$ is at least one order of magnitude smaller than the interaction term associated with the $1s\sigma ns\sigma$ configuration. The proportion of the active configuration is inserted in Eq. 14. This diabatic crossing is also present for the $g, h\ ^3\Sigma_g^+$ states which have an avoided crossing at ~ 2 Bohr radii (see Fig. 1 in the main text, and (*23, 24*)).

The partial cross sections are computed over the 0.01–1000 eV range of collision energies. Such bounds were chosen because: Below the lower bound the cross section varies as $1/E_{coll}$, see e.g. (*1, 25*), and the branching fraction remains constant. Around the upper bound, the Landau-Zener model ceases to be valid (*26*), as the velocity of the atoms is no longer negligible compared to the velocity of the bound electrons.

Supplementary Note 3.1: Collision energy dependent MN cross sections

The relative cross sections are obtained by evaluating the count rates of events in the biased region (matched velocities) and the unbiased region (unmatched velocities) of the merged beam

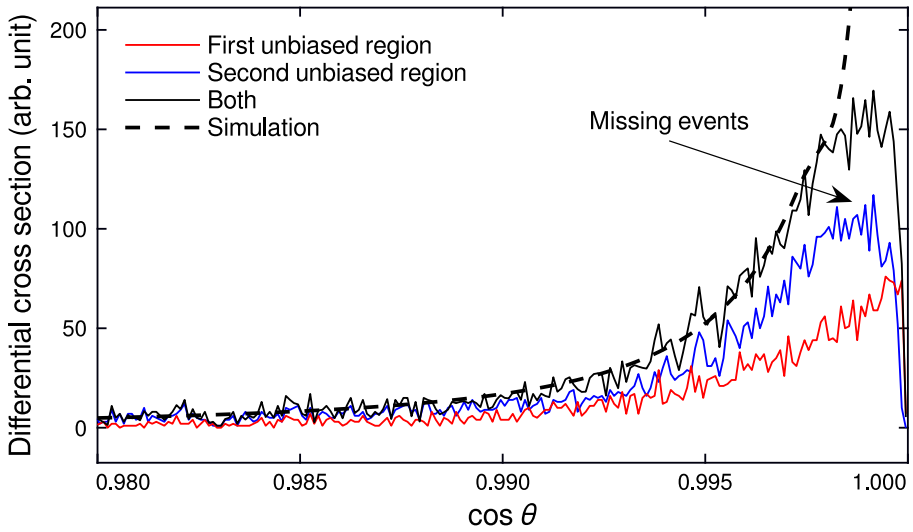

Supplementary Figure 8: Two-body mutual neutralization experimental angular distribution and theoretical differential cross section. The red and blue lines plot the angular distribution coming from the first unbiased region situated between the biased region and the detector, and the second unbiased region before the biased region, respectively; the solid black line plots their sum; the dashed line plots the simulated differential cross section.

section and taking the ratio between them. Here, a different issue must be considered. Even though each pixel of the camera system is triggered independently, i.e., there is no dead time between different pixels, each pixel has its own dead time of 10 μs. Thus, if two products collide on the same pixel (i.e. $\cos\theta \equiv v\Delta t/|\vec{r}| > 0.995$), the second one is not detected, and the coincidence is not triggered. At low collision energies, this effect is negligible as the angular differential cross section distribution is nearly isotropic. However, for two-body MN events occurring in the unbiased region, $E_{coll} \sim 19.3$ eV, and the differential cross section tends to a delta function around $\cos\theta = 1$. Considering that all collisions are initially aligned with the beam propagation axis implies that the two neutral particles separate along a line which is nearly perpendicular to the normal to the detector surface. This requires knowledge of the differential cross section. Here, the latter is estimated using the impact parameter model described earlier. These aspects are illustrated in Supplementary Fig. 8. With these data, total cross sections are

obtained on a relative scale. Finally, all data points are normalized on the two-body signal from the unbiased region fixed at $9.2\times\ 10^{-15}$ cm^2 for comparison with theoretical calculations.

Supplementary Note 3.2: Partial rate coefficients

Using the computed total and partial cross section data, the temperature-dependent rate coefficients for the MN reaction of H_2^+ + H^- can be determined for a range of temperatures. Here, the partial rates for each of the states involved in the reaction are obtained, and Supplementary Fig. 9 plots rate-coefficient data for the total reaction, as well all the contributions for all of the states considered in the model. The data are calculated up to an effective temperature of 20,000 K. In the best-fit to the data presented in the main manuscript, only the total of the dissociative and non-dissociative channels at their sum were included.

The partial rate coefficient k leading to a neutral electronic state n at a temperature T is given by:

$$k(n,T) = \sqrt{\frac{8}{\pi\mu(k_BT)^3}} \sum_{v_0} \sum_{v_+} p(v_+) \int_{10^{-7}\ \mathrm{eV}}^{10^{3}\ \mathrm{eV}} \sigma(E_{coll}, n, v_0, v_+) e^{-E_{coll}/kT} E_{coll}\ \mathrm{d}E_{coll} \quad (16)$$

where μ is the reduced mass, k_B is the Boltzmann constant, $\sigma(E_0, n, v_0, v_+)$ is the cross section from the cation vibrational state v_+ to the neutral vibrational state v_0, and $p(v_+)$ is the thermal cation vibrational population:

$$p(v_+) = \frac{e^{-E_{v_+}/(k_BT)}}{\sum_{v'_+} e^{-E_{v'_+}/(k_BT)}} \quad (17)$$

where E_{v_+} is vibrational excitation energy of the cation. The cross section was extended below 1 meV using its analytical $1/E_{coll}$ dependency at such low collision energies. This was done in order to describe accurately the low temperature regime, and ensure that lower collision energies were not required from the calculation.

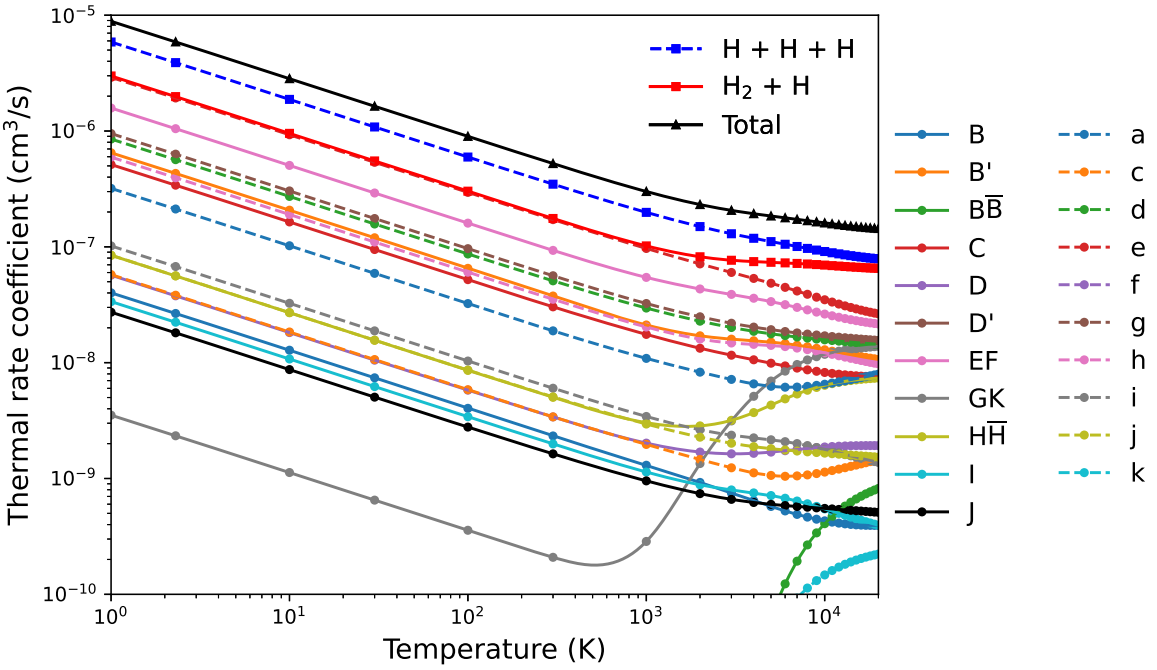

Supplementary Figure 9: Temperature dependent $H_2^+ + H^-$ mutual neutralization rate coefficients for the total reaction, together with all the partial rate coefficients for the individual dissociative and non-dissociative channels included in the current model.

Supplementary References

1. A. Dochain, V. M. Andrianarijaona, and X. Urbain. Isotope effect for the mutual neutralization reaction at low collision energies: $\mathrm{He}^+ + \mathrm{H}^-$. *Phys. Rev. A*, 108:042809, (2023).

2. R. D. Thomas, H. T. Schmidt, G. Andler, M. Björkhage, M. Blom, L. Brännholm, E. Bäckström, H. Danared, S. Das, N. Haag, P. Halldén, F. Hellberg, A. I. S. Holm, H. A. B. Johansson, A. Källberg, G. Källersjö, M. Larsson, S. Leontein, L. Liljeby, P. Löfgren, B. Malm, S. Mannervik, M. Masuda, D. Misra, A. Orbán, A. Paál, P. Reinhed, K.-G. Rensfelt, S. Rosén, K. Schmidt, F. Seitz, A. Simonsson, J. Weimer, H. Zettergren, and H. Cederquist. The double electrostatic ion ring experiment: A unique cryogenic electrostatic storage ring for merged ion-beams studies. *Rev. Sci. Instrum.*, 82:065112, (2011).

3. H. T. Schmidt, R. D. Thomas, M. Gatchell, S. Rosén, P. Reinhed, P. Löfgren, L. Brännholm, M. Blom, M. Björkhage, E. Bäckström, J. D. Alexander, S. Leontein, D. Hanstorp, H. Zettergren, L. Liljeby, A. Källberg, A. Simonsson, F. Hellberg, S. Mannervik, M. Larsson, W. D. Geppert, K. G. Rensfelt, H. Danared, A. Paál, M. Masuda, P. Halldén, G. Andler, M. H. Stockett, T. Chen, G. Källersjö, J. Weimer, K. Hansen, H. Hartman, and H. Cederquist. First storage of ion beams in the Double Electrostatic Ion-Ring Experiment: DESIREE. *Rev. Sci. Instrum.*, 84:055115, (2013).

4. Thibaut Launoy, Jérôme Loreau, Arnaud Dochain, Jacques Liévin, Nathalie Vaeck, and Xavier Urbain. Mutual Neutralization in Li^+-D^- Collisions: A Combined Experimental and Theoretical Study. *The Astrophysical Journal*, 883:85, (2019).

5. H. T. Schmidt, G. Eklund, K. C. Chartkunchand, E. K. Anderson, M. Kamińska, N. de Ruette, R. D. Thomas, M. K. Kristiansson, M. Gatchell, P. Reinhed, S. Rosén, A. Simonsson, A. Källberg, P. Löfgren, S. Mannervik, H. Zettergren, and H. Cederquist. Erra-

tum: Rotationally Cold OH^- Ions in the Cryogenic Electrostatic Ion-Beam Storage Ring DESIREE [Phys. Rev. Lett. 119, 073001 (2017)]. *Phys. Rev. Lett.*, 121:079901, (2018).

6. Z. Amitay, D. Zajfman, and P. Forck. Rotational and vibrational lifetime of isotopically asymmetrized homonuclear diatomic molecular ions. *Phys. Rev. A*, 50:2304–2308, (1994).

7. Mathias Poline, Arnaud Dochain, Stefan Rosén, Mingchao Ji, Henrik Cederquist, Henning Zettergren, Henning T Schmidt, Mats Larsson, Shaun G Ard, Nicholas S Shuman, Albert A Viggiano, and Richard D Thomas. Vibrationally-dependent molecular dynamics in mutual neutralisation reactions of molecular oxygen ions. *Nature Communications*, 16(1):8528, (2025).

8. A. Nomerotski, M. Chekhlov, D. Dolzhenko, R. Glazenborg, B. Farella, M. Keach, R. Mahon, D. Orlov, and P. Svihra. Intensified Tpx3Cam, a fast data-driven optical camera with nanosecond timing resolution for single photon detection in quantum applications. *Journal of Instrumentation*, **18**:C01023, (2023).

9. M. Fisher-Levine and A. Nomerotski. TimepixCam: a fast optical imager with time-stamping. *Journal of Instrumentation*, **11**:C03016, (2016).

10. Mathias Poline, Arnaud Dochain, Stefan Rosén, MingChao Ji, Peter Reinhed, Ansgar Simonsson, Mats Larsson, Henning T. Schmidt, Henning Zettergren, Richard D. Thomas, Shaun G. Ard, Nicholas S. Shuman, and Albert A. Viggiano. Mutual Neutralization of NO^+ with O^-. *Phys. Rev. Lett.*, 132:023001, (2024).

11. Akiyoshi Hishikawa, Hirokazu Hasegawa, and Kaoru Yamanouchi. Sequential three-body Coulomb explosion of CS_2 in intense laser fields appearing in momentum correlation map. *Chemical Physics Letters*, 361:245–250, (2002).

12. Mathias Poline, Arnaud Dochain, Stefan Rosén, Jon Grumer, MingChao Ji, Gustav Eklund, Ansgar Simonsson, Peter Reinhed, Mikael Blom, Nicholas S. Shuman, Shaun G. Ard, Albert A. Viggiano, Mats Larsson, Henrik Cederquist, Henning T. Schmidt, Henning Zettergren, Xavier Urbain, Paul S. Barklem, and Richard D. Thomas. Mutual neutralisation of O^+ with O^-: investigation of the role of metastable ions in a combined experimental and theoretical study. *Phys. Chem. Chem. Phys.*, 23:24607–24616, (2021).

13. U. Fantz and D. Wünderlich. Franck–Condon factors, transition probabilities, and radiative lifetimes for hydrogen molecules and their isotopomeres. *Atomic Data and Nuclear Data Tables*, 92:853–973, (2006).

14. L. D. Landau. On the theory of transfer of energy at collisions II. *Phys. Z. Sowjetunion*, 2(46-51):118, (1932).

15. Clarence Zener and Ralph Howard Fowler. Non-adiabatic crossing of energy levels. *Proc. Math. Phys. Eng. Sci.*, 137:696–702, (1932).

16. Paul S. Barklem, Anish M. Amarsi, Jon Grumer, Gustav Eklund, Stefan Rosén, MingChao Ji, Henrik Cederquist, Henning Zettergren, and Henning T. Schmidt. Mutual Neutralization in Li^++H^-/D^- and Na^++H^-/D^- Collisions: Implications of Experimental Results for Non-LTE Modeling of Stellar Spectra. *The Astrophysical Journal*, 908:245, (2021).

17. A. Salop and R. E. Olson. Charge exchange between $\mathrm{H}(1s)$ and fully stripped heavy ions at low-keV impact energies. *Phys. Rev. A*, 13:1312–1320, (1976).

18. Conyers Herring. Critique of the Heitler-London Method of Calculating Spin Couplings at Large Distances. *Rev. Mod. Phys.*, 34:631–645, (1962).

19. R. K. Janev and A. R. Tancic. Recombination of H^+ and H^- ions in slow collisions. *Journal of Physics B: Atomic and Molecular Physics*, 5:L250–L252, (1972).

20. *NIST Digital Library of Mathematical Functions*. `https://dlmf.nist.gov/`, Release 1.2.2 of 2024-09-15. F. W. J. Olver, A. B. Olde Daalhuis, D. W. Lozier, B. I. Schneider, R. F. Boisvert, C. W. Clark, B. R. Miller, B. V. Saunders, H. S. Cohl, and M. A. McClain, eds.

21. C. L. Liu, J. G. Wang, and R. K. Janev. Mutual neutralization in slow H_2^+-H^- collisions. *Journal of Physics B: Atomic, Molecular and Optical Physics*, 39:1223, (2006).

22. Åsa Larson, Patrik Hedvall, Michael Sahlin, Marjan Khamesian, and Ann E Orel. Theoretical studies of charged particle collisions. *Journal of Physics: Conference Series*, 1412:062004, (2020).

23. Charles B. Wakefield and Ernest R. Davidson. Some Triplet States of the Hydrogen Molecule. *The Journal of Chemical Physics*, 43:834–839, (1965).

24. Keld Lars Bak and Jan Linderberg. Nonadiabatic abinitio calculations of eigenfunctions and energies for the 3s,3d-triplet complex of molecular hydrogen. *The Journal of Chemical Physics*, 92:3668–3679, (1990).

25. H. R. Sadeghpour, J. L. Bohn, M. J. Cavagnero, B. D. Esry, I. I. Fabrikant, J. H. Macek, and A. R. P. Rau. Collisions near threshold in atomic and molecular physics. *Journal of Physics B: Atomic, Molecular and Optical Physics*, 33:R93, (2000).

26. V. Sidis, C. Kubach, and D. Fussen. Ionic-covalent problem in the H^++$H^-$$\rightleftarrows$$H^*$+H collisional system. *Phys. Rev. A*, 27:2431–2446, (1983).